Advanced Engineering Materials

ADVANCED ENGINEERING MATERIALS
www.aem-journal.com

RESEARCH ARTICLE OPEN ACCESS

Creep-Induced Microstructural Evolution in an A2-B2 Superalloy

Liu Yang[1] | Aparajita Pramanik[2] | Sandipan Sen[1] | Shubhashis Dixit[1] | Marcel Muench[1] | R. J. Vikram[1] | Daniel Schliephake[1] | Yolita M. Eggeler[3] | Ankur Chauhan[2] | Martin Heilmaier[1] | Alexander Kauffmann[4]

[1]Institute for Applied Materials (IAM-WK), Karlsruhe Institute of Technology (KIT), Karlsruhe, Germany | [2]Extreme Environments Materials Group (EEMG), Department of Materials Engineering, Indian Institute of Science (IISc), Bangalore, India | [3]Laboratory for Electron Microscopy (LEM), Karlsruhe Institute of Technology (KIT), Karlsruhe, Germany | [4]Institute for Materials (IM), Ruhr University Bochum (RUB), Bochum, Germany

Correspondence: Sandipan Sen (sandipan.sen@kit.edu) | Ankur Chauhan (ankurchauhan@iisc.ac.in) | Alexander Kauffmann (alexander.kauffmann@rub.de)

Received: 11 December 2025 | **Revised:** 4 May 2026 | **Accepted:** 13 May 2026

Keywords: 3D microstructure | A2–B2 | creep deformation | dislocation–precipitate interaction | refractory high-entropy alloys | superalloys

ABSTRACT

The refractory element-based 27.3Ta-27.3Mo-27.3Ti-8Cr-10Al (at.%) high-entropy alloy with a precipitation-strengthened A2-B2 microstructure exhibits substantial B2 raft formation and a transition in apparent creep exponent near 125 MPa at 1030°C. Using focused ion beam-based 3D sectioning, the B2 precipitates were identified as having a plate-like geometry, characterized by elongation on two orthogonal cut faces and faceting on the third face, a morphology that cannot be resolved by conventional 2D imaging. Electron backscatter diffraction analysis reveals the formation of low-misorientation subgrain structures, consistent with dynamic recovery processes. Transmission electron microscopy (TEM) analyses reveal a change in dislocation–precipitate interaction with increasing applied stress. At low stresses, dislocation climb is confirmed, whereas at high stresses, deformation is likely associated with cross slip of screw dislocations. In the intermediate stress range, deformation is characterized by a combination of climb-controlled dislocation–precipitate interaction, jogged-screw dislocations, and the cutting of B2 precipitates by strongly coupled dislocation pairs. High-resolution scanning TEM further confirms that the A2/B2 interface remains fully coherent across all creep conditions examined, maintaining structural stability under high-temperature deformation.

1 | Introduction

Refractory high-entropy alloys (RHEAs) with body-centered cubic (BCC) crystal structure (Strukturbericht designation A2) have attracted considerable attention as potential candidates for high-temperature applications. Their exceptionally high solidus temperatures $T_{solidus}$, reaching up to 2900°C [1, 2], slow diffusion of the refractory elements [3, 4], and strong solid-solution strengthening enable them to retain remarkable strength even at elevated temperatures [5, 6]. Representative alloys, such as NbMoTaW, have been reported to exhibit outstanding compressive yield strength, for example, approximately 405 MPa at 1600°C under quasi-static loading [5]. In contrast, the state-of-the-art Ni-based superalloy CMSX-4 exhibits a yield strength of below 100 MPa at only 1200°C [7, 8]. This remarkable high-temperature strength highlights their potential as next-generation structural materials, particularly since Ni-based superalloys are fundamentally limited by their γ' solvus (approximately 1280°C, e.g., for CMSX-4) and solidus temperature (approximately 1350°C) [9–11].

Despite their excellent high-temperature strength, single-phase BCC RHEAs exhibit inadequate creep resistance. This limitation is exemplified by the equimolar (single-phase) A2 alloy

Liu Yang and Aparajita Pramanik contributed equally to this study.

TiZrHfNbTa, which exhibits markedly lower creep resistance in the temperature range of 980–1100°C than precipitation-strengthened single-crystal Ni-based superalloys, such as CMSX-4, or even the solid-solution matrix thereof [12, 13]. Such low creep performance can be attributed to a number of aspects, such as the polycrystalline nature of the alloy, the absence of precipitation strengthening, and the microstructural instability arising from the gradual decomposition of A2 into A2 and hexagonal close-packed (HCP, Strukturbericht designation A3) phases during prolonged thermal exposure [13]. It should be noted that BCC high-entropy alloys can exhibit relatively higher effective diffusivities at comparable homologous temperatures T/T_{solidus} compared to their FCC counterparts, a trend further amplified by the pronounced lattice distortion effects characteristic of these systems [14, 15]. In contrast, Ni-based superalloys achieve creep resistance through their two-phase microstructure consisting of coherent and thermally stable, ordered $L1_2$ particles (γ') embedded in a face-centered cubic (FCC, Strukturbericht designation A1) matrix (γ), which provides effective and sustained precipitation strengthening [11, 16, 17]. This highlights the critical role of thermo-mechanically stable precipitates in maintaining creep resistance. Motivated by this concept, recent studies have successfully introduced ordered B2 precipitates into multicomponent, refractory element-based alloys that combine solid solution and precipitation strengthening [18–20]. However, systematic investigations of their creep behavior and the associated microstructural evolution in such two-phase systems remain limited.

27.3Ta-27.3Mo-27.3Ti-8Cr-10Al (at.%, hereafter TMT-8Cr-10Al) represents a prototypical example, consisting of an A2 matrix with coherent, ordered B2 precipitates. In our previous work [19, 21], phase separation was observed at (1065 ± 5)°C, followed by precipitate ordering at approximately 1055°C. The resulting B2 phase exhibits excellent microstructural stability even after prolonged exposure near the solvus temperature T_{solvus}, which can be attributed to the high T_{solidus} and the intrinsically low diffusivity of the refractory elements [4, 18]. Our recent study showed that the polycrystalline TMT-8Cr-10Al alloy (approximately $0.98T_{\text{solvus}}$) exhibits creep resistance at 1030°C comparable to the single-crystal superalloy CMSX-4 tested at 1050°C (approximately $0.85T_{\text{solvus}}$) at similar stress levels [22, 23]. Moreover, B2 precipitates in ⟨100⟩-oriented grains rafted perpendicular to the compression loading axis, consistent with the behavior reported for Co-based superalloys, which is associated with a positive lattice misfit [24, 25]. These findings highlight the TMT-8Cr-10Al alloy as a model system for exploring the crept microstructure of precipitation-strengthened BCC RHEAs.

Mechanistic insights into RHEAs have so far been derived primarily from single-phase, A2 alloys similar to TiZrHfNbTa and VNbMoTaW [26–28]. A strength plateau between 800 and 1200°C in HfMoNbTaW (as observed in compression testing) is attributed to a shift from screw to edge dislocation-dominated deformation [29]. In addition to these primary processes, secondary mechanisms such as kink-band formation have been reported for room-temperature tensile deformation in $Ti_{35}Zr_{(35-x)}Hf_xNb_{20}Mo_{10}$ alloys, which further redistribute strain and improve fracture resistance [30]. Liu et al. [12] have reported solute drag creep mechanisms in single-phase HfNbTaTiZr within the temperature range of 1100–1250°C and a tensile stress range of 5–30 MPa, where curved dislocations were observed, and deformation is controlled by $\frac{1}{2}\langle 111\rangle$ dislocations. In contrast, a recent study on the tensile creep behavior of the $Nb_{45}Ta_{25}Ti_{15}Hf_{15}$ RHEA at 900°C and stresses between 50–300 MPa has reported an apparent stress exponent of 4.1. Creep deformation is revealed to be controlled by cross-kink collisions from screw dislocations, leading to dipole drag at lower strain rate and jog drag at higher strain rate [31]. The B2 phase often acts as a strengthening phase in high-temperature alloys. In binary B2 intermetallics, such as NiAl [32] and TiFe [33], the deformation behavior has been systematically investigated, providing valuable insights into their slip systems and strength anomaly phenomena [34–37]. In Al-containing RHEAs, however, the role of the B2 phase becomes considerably more complex. In addition to its intrinsic stability, the strengthening efficiency strongly depends on the antiphase boundary (APB) energy, which governs how dislocations interact with ordered precipitates [38, 39]. For the presently investigated TMT-8Cr-10Al alloy, the APB energy was estimated to be (150 ± 39) mJ/m^2 at room temperature [40].

Our previous work investigated the creep behavior of the TMT-8Cr-10Al alloy in the temperature range of 1000–1060°C and at applied stresses of 75–175 MPa [21]. Two distinct regimes were identified: a high-creep-resistance (HCR) regime at lower temperatures and a low-creep-resistance (LCR) regime at higher temperatures. Temperatures at and above 1040°C fall within the LCR regime, where the creep strength decreases markedly due to partial dissolution of the B2 phase as the temperature approaches the solvus temperature of (1065 ± 5)°C, leading to a significant reduction in the B2 volume fraction [21]. In contrast, the alloy exhibits superior creep resistance at or below 1030°C in the HCR regime, which is comparable to that of single-crystalline CMSX-4 tested under similar conditions. However, the dislocation–precipitate interaction and the evolution of the A2/B2 interface during creep remain unknown. In this study, we address this gap with the two-phase RHEA TMT-8Cr-10Al. Samples were examined at 1030°C under applied stresses of 100, 125, and 150 MPa, with the 125 MPa condition marking a transition in the apparent creep exponent, suggesting a change in deformation behavior. Therefore, three specific research questions will guide this study:

1. What is the 3D morphology of the rafted B2 precipitates after creep deformation?
2. How do dislocation–precipitate interactions evolve with applied stress during creep?
3. How does the A2/B2 interface evolve under creep, and does it retain atomic-scale coherency across different stress conditions?

By clarifying these aspects, this study reveals the complex 3D architecture of the rafted B2 precipitates and elucidates the link between dislocation-precipitate interactions and macroscopic creep resistance, providing a basis for the microstructural design of advanced high-temperature alloys.

2 | Materials and Experimental Methods

The TMT-8Cr-10Al alloy was fabricated by repetitive arc melting under argon atmosphere using an AM/0.5 arc melter (Edmund Bühler GmbH, Germany). High-purity elemental constituents Ta (99.9%), Mo (99.95%), Ti (99.8%), Cr (99.99%), and Al (99.99%) were supplied by chemPUR GmbH (Germany). Two batches of approximately 120 g of alloy were produced through five consecutive melting and flipping cycles to ensure chemical homogeneity. To eliminate the dendritic microstructure, the as-cast alloy was encapsulated in Ta foil and homogenized at 1600°C for 20 h under a constant flow of high-purity Ar. Heating and cooling were controlled at 100 K/h in a HTRH 70-600/18 resistance furnace (Carbolite Gero GmbH & Co. KG, Germany).

For microstructural investigations, cuboidal specimens of size $(5 \times 3 \times 3)\,mm^3$ prepared by electrical discharge machining (EDM) were successively ground with SiC abrasive papers up to P4000 grit and subsequently polished with 3 and 1 µm diamond suspensions, for approximately 5 min each. Afterward, the specimens were polished for 10 min using a colloidal oxide suspension (Buehler ITW, Germany). Final surface preparation was achieved through vibratory chemo-mechanical polishing with a non-crystallizing oxide suspension (Struers, Germany) for a minimum of 16 h. Microstructural characterization was performed using scanning electron microscopy (SEM) in backscattered electron (BSE) mode on a Zeiss LEO 1530 operated at 20 kV. Crystallographic orientation, local strain, and residual stress distributions were analyzed using electron backscatter diffraction (SEM-EBSD) with an EDAX Digiview detector mounted on a Zeiss Auriga 60 SEM.

Compression creep specimens with dimensions of $(5 \times 3 \times 3)\,mm^3$ were also prepared by EDM and subsequently ground with SiC abrasive papers up to P2500 grit to remove any oxide and EDM surface layers. Care was taken to ensure that the top and bottom faces of each specimen were strictly parallel to guarantee uniform stress distribution during testing. Compression creep tests were then performed under vacuum (5×10^{-5} mbar) using a Z100 electro-mechanical testing system (ZwickRoell GmbH & Co. KG, Germany) equipped with a Maytec high-temperature vacuum furnace. Specimens were tested at 1030°C under applied true stresses ranging from 100 to 150 MPa. Prior to loading, each specimen was held at the target temperature for 30 min under a 50 N preload to ensure uniform temperature distribution and thermal stability, while maintaining a constant loading rate of 30 MPa/min. After deformation, the specimens were furnace-cooled to room temperature and subsequently prepared for microstructural characterization following the metallographic procedures described above. To ensure reproducibility, at least three independent creep tests were performed for each stress condition. For quantitative analysis of the creep behavior, the minimum (or steady-state, if present) creep rate is commonly expressed by the classical power-law creep equation [41]:

$$\dot{\varepsilon}_{min} = A\,\sigma^{n}\,\exp\left(-\frac{Q}{RT}\right) \tag{1}$$

where $\dot{\varepsilon}_{min}$ is the minimum creep rate, σ is the applied stress, n is the apparent stress exponent reflecting the sensitivity of creep rate to stress, Q is the apparent activation energy, R is the universal gas constant, and T is the absolute temperature. The parameter A is a material constant that depends on factors such as elastic modulus, diffusion coefficient, and dislocation density. In the present alloy system, our previous study demonstrated that, under the investigated conditions (100–150 MPa, 1030°C), the creep behavior enters a steady-state regime [21]. This steady-state creep rate was therefore designated as the minimum creep rate, as it corresponds to the lowest strain rate observed during the creep experiment.

To directly visualize the three-dimensional (3D) morphology of the B2 precipitates, a creep sample with a representative grain orientation was selected, and a quasi-3D representation was constructed based on orthogonal FIB sections. A grain oriented close to ⟨100⟩ parallel to the compression direction was chosen, as this orientation has previously been reported to exhibit N-type rafting behavior under creep conditions [21]. Focused ion beam (FIB) milling was employed to cut a site-specific micropillar from such a grain using a Thermo Fisher Helios G4-dual beam system. The micropillar was oriented to expose the top, lateral, and front surfaces of the same grain, allowing a comprehensive assessment of precipitate morphology along different crystallographic directions. During FIB preparation, a protective Pt layer (approximately 1 µm thick) was first deposited to prevent ion-induced damage. Subsequent coarse milling was carried out at 30 kV with a beam current of 21 nA, followed by a final polishing step at 2.4 nA to minimize surface artifacts. All micrographs were recorded using an in-column BSE detector, while operating in immersion mode.

Crept samples were analyzed by SEM-EBSD using a Thermo Fisher Scientific Helios G4-UX SEM equipped with an EDAX detector. Standard SEM-EBSD maps were acquired at an accelerating voltage of 30 kV, a probe current of 13 nA, with a step size of 0.5 µm, which sets the spatial resolution of these scans. The acquired data were analyzed using TSL OIM version 8.0 software.

Transmission electron microscopy (TEM) lamellae were prepared from crept specimens (1030°C for 100, 125, and 150 MPa) using the same site-specific FIB approach, with lift-outs taken from the grains close to ⟨100⟩ orientation, as identified from SEM-EBSD maps. The milling parameters were adjusted for foil preparation (30 kV bulk milling, final cleaning at 2 kV/27 pA). Subsequent diffraction-contrast imaging was conducted using a Thermo Fisher Tecnai F30 TEM operated at 300 kV. TEM selected area diffraction patterns (TEM-SADPs) and dark-field (TEM-DF) imaging were used to identify and characterize the precipitates, while two-beam TEM bright-field (TEM-BF) imaging enabled visualization of dislocations and their interactions with the precipitates. The TEM-DF micrographs used to reveal the B2 precipitates were obtained using the {100} superlattice reflection under a ⟨001⟩ zone-axis condition of the A2 matrix. A ⟨001⟩ zone axis (ZA) was specifically selected to enable clearer visualization of the rafted B2 precipitates. Dislocation imaging, in contrast, was performed under two-beam conditions corresponding to ⟨001⟩ and ⟨113⟩ zone axes of A2. High-resolution scanning TEM (STEM) investigations were performed in a probe-corrected Titan Themis (300 kV) using a high-angle annular dark-field (STEM-HAADF) detector. Atomic-resolution STEM-HAADF micrographs were acquired with a camera length of 160 mm, and image drift during

acquisition was compensated by using the drift-corrected frame integration function in Velox software.

3 | Results and Discussion

3.1 | Composition and Initial Microstructure

The nominal composition of TMT-8Cr-10Al is shown in Table 1. The experimentally determined concentrations of the two alloy batches, measured by SEM-EDS, deviate only slightly from the target values, confirming that the alloy was produced close to its designed composition [19]. The O and N contents of the two batches are within the range typically reported for RHEAs [19, 42, 43]. The experimental density of this alloy measured by the Archimedes method is 9.6 g cm^{-3} [21].

Figure 1 presents the initial homogenized microstructure of the alloy. Figure 1a shows the kernel average misorientation (KAM) map, which helps visualize local variations in crystallographic orientation and highlights regions with a high density of geometrically necessary dislocations within grains. It is evident from Figure 1a that the homogenized and furnace-cooled microstructure exhibits relatively low local misorientation, as indicated by predominantly low KAM values (i.e., blue color). The inverse pole figure map (Figure S1) confirms a random grain orientation distribution, indicating the absence of crystallographic texture. The average grain size is approximately (620 ± 180) μm, which is considered sufficiently coarse, such that grain-boundary sliding does not make a significant contribution to creep deformation [21]. Figure 1b shows the grain boundary character map overlaid on the image quality (IQ) map of the same region shown in Figure 1a. Although most of the grain boundaries observed in Figure 1b are high-angle grain boundaries with misorientation >15°, there are a few low-angle grain boundaries (8°–12°) that remain even after the homogenization. At higher magnification, the SEM-BSE micrograph in Figure 1c, obtained within a grain, shows dark-contrast precipitates clearly distinguished from the bright matrix. Based on earlier diffraction and chemical analyses [18, 21], the bright regions correspond to a disordered A2 matrix phase enriched in Ta and Mo. In contrast, the dark regions are identified as ordered B2 precipitates, enriched in Al and Ti, with Cr distributed homogeneously between the two phases. The B2 precipitates, formed via a precipitation reaction, are uniformly distributed, with an average size of 10–20 nm and a volume fraction of around 20% [18, 19]. The observed two-phase microstructure serves as the initial condition for subsequent creep experiments.

3.2 | Creep Behavior at 1030°C

Figure 2a presents the double-logarithmic plot of minimum creep rate as a function of applied stress at 1030°C for stresses ranging from 75 to 175 MPa. In the previously reported dataset [21], the creep curves at lower stress conditions (75 and 100 MPa) only approached steady state without fully reaching it. If these tests had continued longer, the resulting creep rates might have been slightly lower, and consequently, the apparent stress exponent somewhat higher. To improve the statistical robustness of these low-stress conditions, additional creep tests were performed in the present study at 75 and 100 MPa, successfully achieving complete steady state. When these new datapoints, along with the data reported in Ref. [21], are plotted together, an apparent stress exponent of approximately 3.5 is observed. While slightly lower than the previously reported 4.3 [21], this observed stress exponent remains consistent with matrix-controlled creep governed by dislocation climb [44].

In the higher-stress conditions (125 to 175 MPa), the data deviate markedly from the low-stress trend, yielding an apparent stress exponent of approximately 19. This transition suggests a fundamental change in the underlying deformation behavior, potentially involving microstructural instabilities or changes in dislocation-precipitate interactions, such as precipitate cutting, Orowan bypassing and cross slip [45, 46].

Based on this stress-dependent transition, three representative conditions (100, 125, and 150 MPa) were selected for detailed microstructural characterization and investigation of dislocation–precipitate interaction. Figure 2b shows the corresponding creep strain rate versus creep strain curves. The specimen tested at 100 MPa remains within the primary creep region, approaching the onset of steady-state creep, whereas the specimens tested at 125 MPa and 150 MPa are well within the steady-state conditions.

3.3 | B2 Precipitates—Morphology and Subgrain Structure Evolution During Creep

Figure 3a–c shows SEM-BSE micrographs of the TMT-8Cr-10Al alloy crept at 1030°C under applied stresses of 100, 125, and 150 MPa, respectively. The compression axis in the micrographs is oriented horizontally. Compared with the initial microstructure, in which the B2 precipitates exhibit a nearly spherical morphology and a random spatial distribution, the crept samples show pronounced coarsening and directional alignment of the precipitates (i.e., rafting). Rafting is observed across all investigated conditions, though its extent does not scale solely with the applied stress. While a more continuous rafting morphology

TABLE 1 | Target and experimental composition (at.%) and impurity levels (wt.-ppm) of the investigated alloy batches [21].

	Ta	Mo	Ti	Cr	Al	O	N
			at.%			wt.-ppm	
Target	27.3	27.3	27.3	8.0	10.0	—	—
Experimental (Batch 1)	26.0	29.8	27.4	7.3	9.4	352 ± 88	45 ± 14
Experimental (Batch 2)	26.8	30.5	26.8	7.0	8.9	248 ± 50	31 ± 8

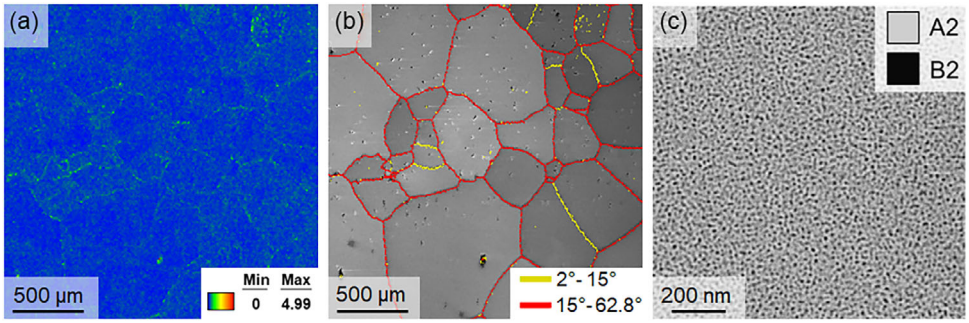

FIGURE 1 | Initial meso- and microstructure of the homogenized and furnace-cooled material. (a) KAM map; (b) grain boundary character map overlayed with IQ map from the same region; and (c) high-magnification SEM-BSE micrograph revealing A2 matrix (bright contrast) and B2 precipitates (dark contrast).

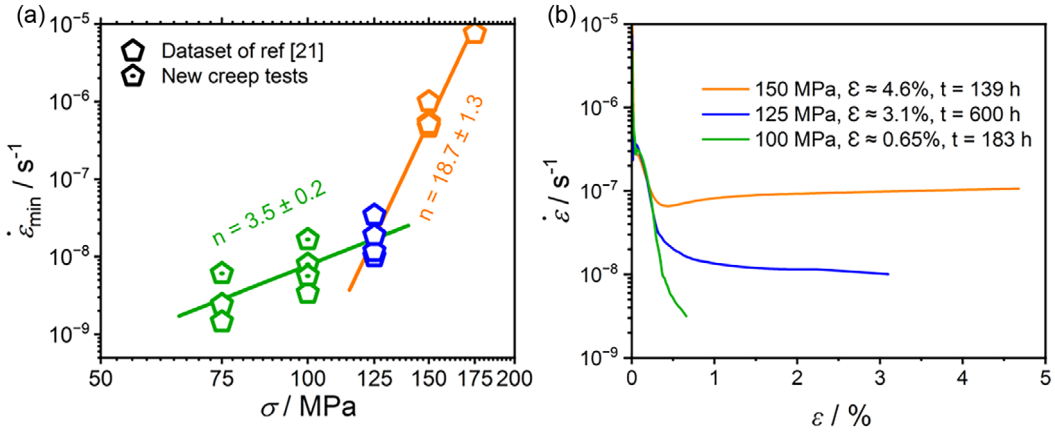

FIGURE 2 | Compilation of relevant creep data. (a) double-logarithmic plot of minimum creep rate versus applied stress between 75 and 175 MPa at 1030°C, with each symbol representing the result of an individual creep sample. Open pentagons with a central dot denote data from new creep tests in this study, while open pentagons denote data from Ref. [21]; and (b) creep rate versus creep strain of selected specimens tested at 100, 125, and 150 MPa, which were used for subsequent TEM investigations.

is apparent at 100 MPa as compared to the higher stress levels, this cannot be directly attributed to the lower stress level alone; rather, it is a process dependent on both time and strain, as noted by Kamaraj et al. [47]. The grains shown in these micrographs are oriented close to ⟨100⟩ crystallographic direction parallel to the compression axis. As demonstrated in our previous study, only grains with this specific orientation develop B2 rafts aligned perpendicular to the loading axis in the polycrystalline alloy [21]. Given the strong orientation dependence of rafting and deformation behavior, the present analysis focuses on ⟨100⟩-oriented grains.

While the SEM-BSE observations provide valuable insights into the post-creep morphology of the B2 precipitates, they represent only 2D sections of the underlying 3D microstructure. To visualize the spatial morphology of the rafted precipitates, a specimen crept at 1030°C under 150 MPa with a total strain of 7.8% was selected, as it provided sufficiently long rafted precipitates for analysis.

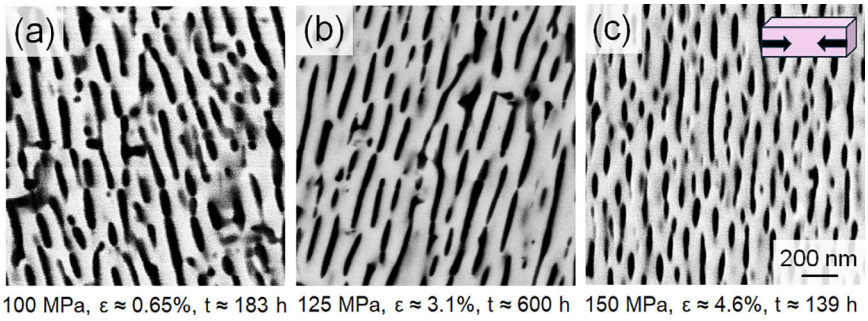

FIGURE 3 | SEM-BSE micrographs of TMT-8Cr-10Al creep tested at 1030°C under different applied stresses: (a) 100 MPa, ε ≈ 0.65%, t ≈ 183 h; (b) 125 MPa, ε ≈ 3.1%, t ≈ 600 h; and (c) 150 MPa, ε ≈ 4.6%, t ≈ 139 h.

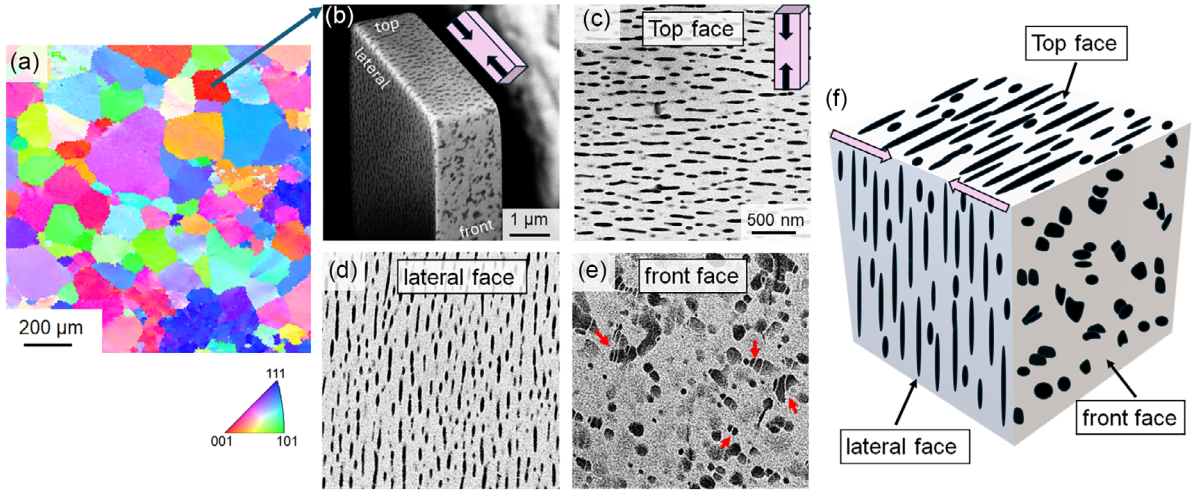

FIGURE 4 | (a) EBSD IPF map of the specimen crept at 1030°C and 150 MPa; (b) site-specific FIB cross-section and micropillar preparation from the selected ⟨100⟩ grain, ICD micrographs of the micropillar acquired from three orthogonal views; (c) top surface; (d) lateral face; (e) front face; and (f) quasi-3D representation showcasing the morphology of the B2 precipitates.

The selected ⟨100⟩ grain orientation was identified by SEM-EBSD (Figure 4a), followed by site-specific FIB cross-sectioning (Figure 4b) and fabrication of a micropillar for microstructural analysis. In-column detector (ICD) micrographs were then acquired from three orthogonal views of the micropillar (top, lateral, and front faces), as shown in Figure 4c–e.

Based on these orthogonal views, a quasi-3D representation of the precipitate morphology in the ⟨100⟩-oriented grain was generated, as shown in Figure 4f. This representation reveals that the B2 precipitates adopt a plate-like geometry aligned perpendicular to the loading direction. On the top and lateral face, the precipitates appear as elongated plates, while the front faces display near-circular cross-sections, respectively, indicating that the plates are continuous and laterally interconnected. The apparent cut-through features marked by red arrows in Figure 4e are the remaining gaps between the growing and rafted B2 precipitates, which are about to join.

To examine the deformation behavior at the micrometer scale, SEM-EBSD analyses were performed (same step size as for Figure 1) on the crept samples corresponding to creep curves in Figure 2b. Figure 5a–c shows the KAM maps for the three creep conditions. Compared to the homogenized condition (Figure 1), all crept samples exhibit increased local misorientation, reflecting the accumulation of plastic strain during creep. The magnitude and spatial heterogeneity of the misorientation increase with applied stress and total creep strain, with higher local misorientation frequently observed near grain boundaries.

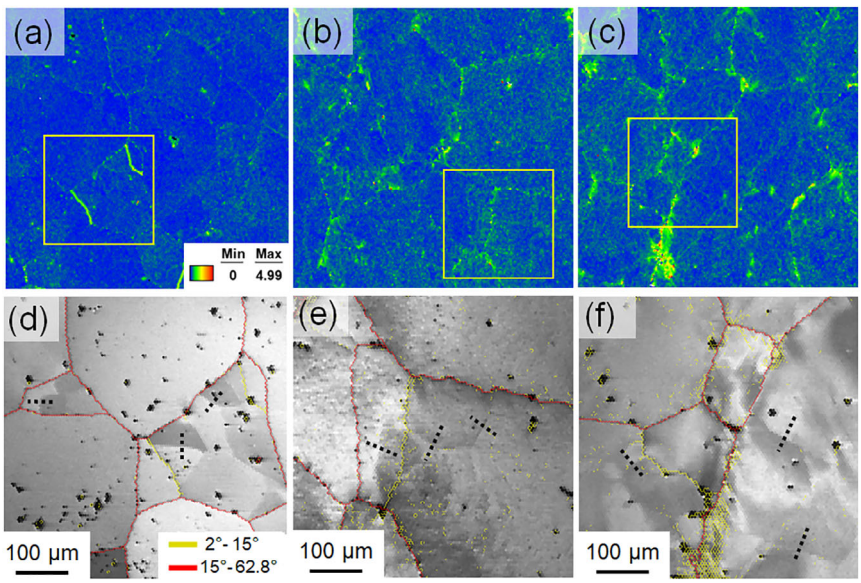

FIGURE 5 | EBSD maps of TMT-8Cr-10Al after creep at 1030 °C: (a–c) KAM map showing enhanced local misorientation for samples crept at 100, 125, and 150 MPa, respectively; and (d–f) grain boundary character map overlayed with IQ map of a smaller region (highlighted by a yellow box in a–c), indicating LAGBs (yellow) and HAGBs (red). black dotted lines are drawn across the subgrain boundaries (SGBs) formed during creep deformation.

To further assess the development of deformation substructures, grain boundary character maps were overlaid with IQ maps for selected regions (Figure 5d–f). In addition to preexisting high-angle grain boundaries (HAGBs), low-angle grain boundaries (LAGBs) with misorientations of 8°–12° are observed in both the homogenized and crept conditions. However, the IQ maps also reveal the formation of finer subgrain structures within the grains under all creep conditions.

To quantify these features, point-to-origin misorientation profiles were extracted across selected subgrain boundaries (SGBs), as indicated in Figure 5d–f. The measured misorientations across these SGBs range from approximately 0.6° to 1.2°. As this is significantly lower than the misorientations of the preexisting LAGBs in the homogenized and furnace-cooled condition, these SGB must develop during creep deformation.

The formation of such low-misorientation subgrain structures is consistent with dynamic recovery processes, involving the rearrangement of dislocations into energetically favorable configurations. The observed subgrains shown in Figure 5d–f exhibit average sizes exceeding 50–100 μm, dependent also on the size of the grain in which they form. A detailed description of the point-to-origin misorientation maps is provided in the Figure S2.

3.4 | Dislocation Structure and Interaction with B2 Precipitates During Creep

To examine dislocation morphology and dislocation–precipitate interactions as a function of creep stress, TEM was performed on specimens crept at three different stress levels. The analysis focused on grains oriented with ⟨001⟩ almost parallel to the compression axis, where pronounced N-type rafting was observed.

3.4.1 | Low-Stress Condition at 100 MPa

Figure 6a shows the TEM-SADP acquired along a [001] ZA from the specimen crept at 1030°C and 100 MPa, displaying weak B2 superlattice peaks alongside the fundamental A2/B2 spots. The corresponding TEM-DF micrograph in Figure 6b, obtained using a B2 superlattice reflection, reveals the B2 precipitates in bright contrast against the darker A2 matrix. The B2 precipitates exhibit an elongated, rafted morphology along ⟨100⟩, consistent with the established orientation relationship $\langle 001\rangle_{B2} \| \langle 001\rangle_{A2}$ and $\{001\}_{B2} \| \{001\}_{A2}$ in this alloy [21].

A low-magnification, two-beam TEM-BF micrograph in Figure 6c provides an overview of the deformed microstructure. Only a few curved dislocations, appearing as dark lines, are visible. The precipitates exhibit a weak bright contrast because the imaging conditions differ from those optimized for superlattice contrast. Qualitatively, the overall dislocation density is low, consistent with the limited creep strain (approximately 0.65%). A high-magnification TEM-BF micrograph (Figure 6d) reveals a dislocation segment interacting with a B2 precipitate (indicated by the black arrow). Trace analysis indicates that this dislocation may glide on either $(\bar{1}01)$ with a Burgers vector of $\frac{1}{2}[1\bar{1}1]$ or on (101) with a Burgers vector of $\frac{1}{2}[\bar{1}11]$. The two possibilities cannot

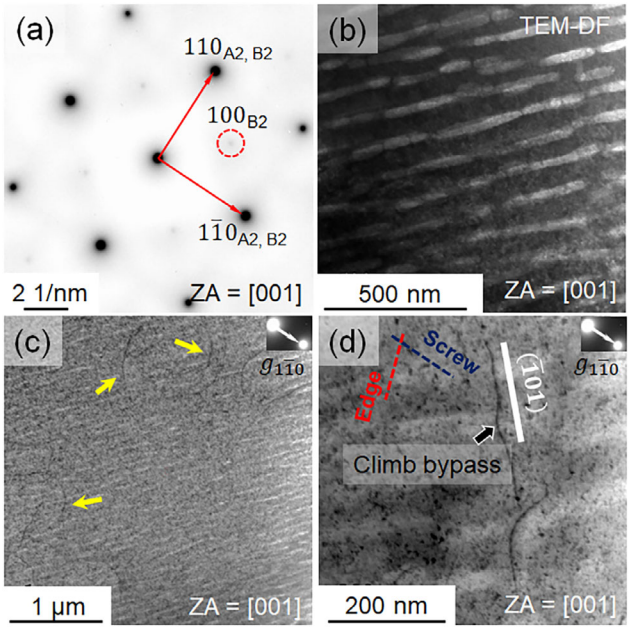

FIGURE 6 | TEM results of the sample crept in the low stress condition (1030°C, 100 MPa): (a) TEM-SADP along a [001] ZA showing the fundamental A2/B2 peaks and weak B2 superlattice spots; (b) TEM-DF micrograph obtained using a [100] B2 superlattice peak reveals bright-contrast B2 precipitates; (c) low-magnification, two-beam TEM-BF micrograph providing an overview of the crept microstructure with few marked curved dislocations; and (d) a relatively high-magnification, two-beam TEM-BF micrograph showing a curved segment of a dislocation (black arrow) bypassing a B2 precipitate via the climb mechanism. The blue and red dashed lines indicate the projection of the screw and edge orientation, respectively; the solid white line indicates the trace of $(\bar{1}01)$ plane.

be distinguished unambiguously due to overlapping traces on the viewing plane (001). To address this, the projected edge and screw orientations were evaluated from the TEM micrograph recorded along the [001] ZA for both possible slip-plane configurations. In both cases, the dislocation exhibits a mixed edge–screw character (in Figure S3), indicating that the curved segment can undergo climb under favorable conditions. An alternative cutting of ordered B2 precipitates can be excluded as it requires the coordinated motion of paired dislocations [48] (as discussed in the next section), whereas only single dislocations are observed in the present case. These observations are therefore consistent with a bypass process involving (local or general) climb [49–51]. This is in agreement with experimental observations on dislocation configurations in B2-strengthened ferritic alloys [52–56] as well as with theoretical considerations by Arzt et al. [57] and Blum et al. [58], who predicted general or local climb configurations always to be rate controlling at low creep stresses.

3.4.2 | Medium-Stress Condition at 125 MPa

Figure 7a shows the TEM-SADP acquired along a [001] ZA from the specimen crept at 1030°C under an intermediate stress of 125 MPa, displaying both the fundamental A2/B2 peaks and the B2 superlattice spots. The corresponding TEM-DF micrograph in Figure 7b, obtained using a [100] B2 superlattice spot, highlights elongated B2 precipitates in bright contrast, rafted

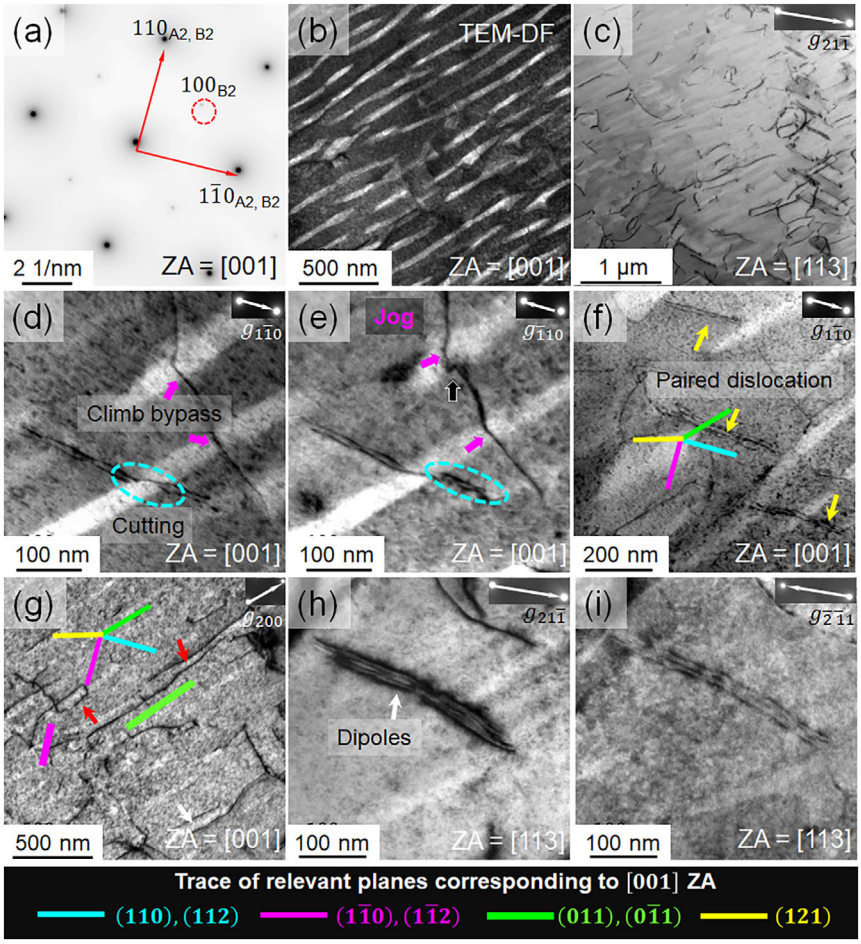

FIGURE 7 | TEM results of the sample crept in the transition stress condition (1030°C, 125 MPa): (a) TEM-SADP along a [001] ZA showcasing the fundamental A2/B2 peaks and weak B2 superlattice spots; (b) TEM-DF micrograph taken using a [100] B2 superlattice peak; (c) low-magnification, two-beam TEM-BF micrograph taken along a [113] ZA presents the overview of the deformed microstructure; (d) two-beam TEM-BF micrograph showing dislocation climb (pink arrows) and superpartial-mediated cutting of a B2 precipitate (ellipse); (e) same area as "d" imaged under reversed diffraction vector (–g), revealing the jogged climb segment (black arrow) and contrast reversal of superpartials within B2; (f) paired dislocations (yellow arrow) near precipitates, indicative of earlier or forthcoming cutting events; (g) long dislocation segments within A2 channels (red arrow), with corresponding trace analysis marked by solid lines; (h) and (i) two-beam TEM-BF micrographs taken under ±g, confirming the presence of dislocation dipoles.

along ⟨100⟩. The low-magnification TEM- BF image in Figure 7c reveals an increased dislocation density compared to the low-stress condition (100 MPa), consistent with the higher creep strain (approximately 3.1%).

A higher-magnification TEM-BF micrograph in Figure 7d shows dislocations interacting with B2 precipitates. In the low-stress condition, a single dislocation exhibits two curved segments (marked by pink arrows) over two precipitates, suggesting bypass of precipitates via climb-assisted motion. Upon tilting the sample to the reversed diffraction condition (–g), as shown in Figure 7e, one of the curved segments exhibits a jog-like configuration (indicated by the black arrow), providing further evidence that climb contributes to the bypass process. The pronounced curvature of the dislocations within the A2 channel (compare Figure 7d,e) further suggests that bypass over the B2 precipitates is slower than glide in the A2 matrix. Additional curved dislocations with cusp-like features in Figure S4 (marked by yellow arrows) resemble jogged screw dislocations, consistent with previous reports [59, 60]. These jog segments can only move along with the parent dislocation via thermally activated climb.

In contrast to the low-stress condition, paired dislocations are frequently observed in Figure 7c and in Figure S4, extending from the A2 matrix into the B2 precipitates (Figure 7d,f). Trace analysis implies that these dislocations lie on {110} or {112} planes (see Figure 7f). To clarify whether these paired dislocations form a dipole (i.e., a pair of dislocations moving on parallel slip planes in opposite directions) or are a set of dislocations with identical Burgers vectors on the same plane, the same region was imaged using the reversed diffraction condition (–g), as shown in Figure 7d,e). The spacing and contrast of paired dislocations in the A2 matrix remain unchanged upon g-reversal, indicating that they lie on the same slip plane and are not dipoles. In contrast, the paired segments within the B2 precipitates exhibit contrast reversal (highlighted by dashed ellipses), suggesting that they correspond to superpartials with identical Burgers vectors gliding on the same slip plane in the ordered phase. One dislocation in each pair exhibits noticeably weaker contrast in Figure 7d, and its contrast reverses under g-reversal in Figure 7e, likely due to elastic interactions between the paired segments [61, 62]. For better visualization, please refer to the overlapped image generated using a color filter in Figure S5. It is important to note that the separation

between the paired dislocations is smaller within the precipitate than in the surrounding A2 matrix, with a clear change in spacing observed across the A2/B2 interface. This indicates cutting of the precipitates by strongly pair-coupled dislocations under this stress condition. Additional instances of paired dislocations near precipitates, likely corresponding to earlier or forthcoming cutting events [63], can be seen in Figure 7f and Figure S4. It is also important to note that the same precipitate appears to interact with both paired dislocations that cut through it and a single dislocation that bypasses it by climb. Therefore, the TEM observations in this intermediate stress condition reveal the coexistence of different dislocation–precipitate interaction modes, including climb-assisted bypass and precipitate cutting by paired dislocations. Additionally, long dislocation segments within the A2 channels are observed in Figure 7g, and trace analysis indicates that they are gliding on {110} or {112} planes. Furthermore, occasional dislocation dipoles are also observed, confirmed by *g*-reversal in Figure 7h,i.

The 125 MPa condition corresponds to intermediate stress where the apparent stress exponent increases from $n \approx 3.5$ to ≈ 19. While this change suggests a transition in deformation behavior, the underlying dominant mechanism cannot be conclusively identified from the present observations. Instead, the coexistence of multiple dislocation-based deformation mechanisms may be associated with this transition [64, 65].

3.4.3 | High-Stress Condition at 150 MPa

The specimen crept at 1030°C under 150 MPa, corresponding to the high-stress condition, with the B2 precipitates remaining rafted along ⟨100⟩, as for the lower stresses (Figure 8a,b).

The low-magnification, two-beam TEM-BF micrograph in Figure 8c provides an overview of the deformed microstructure, revealing long segments of screw or mixed dislocations within the A2 channels. Many of these dislocations exhibit abrupt changes in direction, indicating local changes of glide planes, and thereby forming step-like features (indicated by yellow arrows in Figure 8c). A magnified view of such a configuration, imaged under two diffraction conditions close to [001] and [113] ZA in Figure 8d–e, shows that these features arise from multiple overlapping dislocations. Trace analysis in Figure 8d indicates that the dislocation segments lie on {110} and {112} planes, consistent with the occurrence of cross slip. It should be noted that the dislocation configurations illustrated in Figure 8f can overlap and appear similar to those observed in Figure 8d when viewed along the [001] ZA. The Burgers vector was determined here to be $\frac{1}{2}[\bar{1}11]$ using the visibility–invisibility criterion in Figure S6, with the corresponding two-beam images acquired along the [001] and [113] zone axes. These observations suggest that cross slip of screw (or mixed character) dislocations becomes more prominent under high applied stress (Figure S7). A schematic of the active slip system is provided in Figure S8.

In addition, TEM observation along the [113] ZA (Figure 8g) reveals several dislocation–precipitate interactions (indicated by blue arrows), which resemble the climb-assisted bypass configuration observed at lower stress. This suggests that bypass via climb still occurs locally under high-stress conditions. Notably, no evidence of precipitate cutting by paired dislocations is observed in this condition.

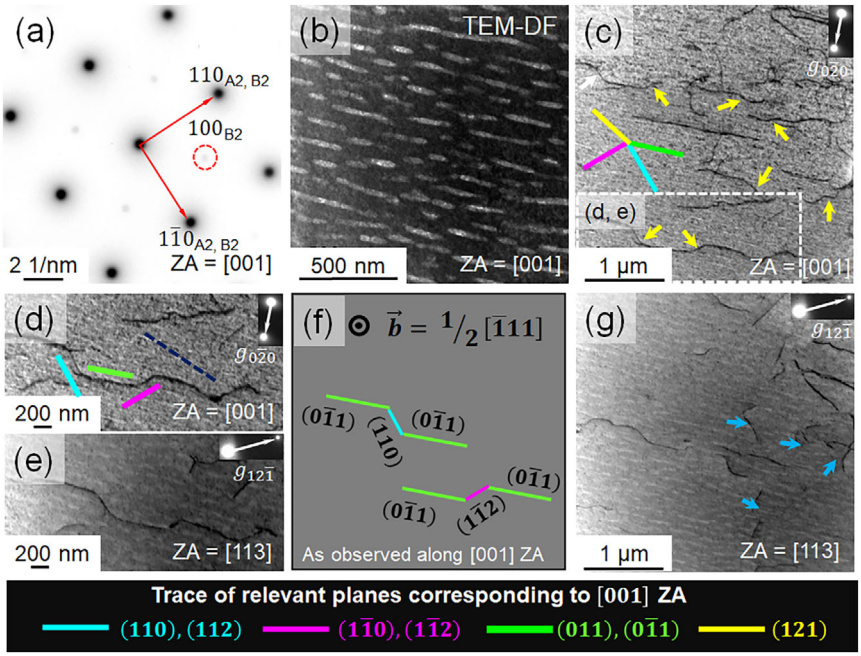

FIGURE 8 | TEM results of the sample crept under high stress condition (1030°C, 150 MPa). (a) TEM-SADP along a [001] ZA showcasing fundamental A2/B2 peaks and weak B2 superlattice spots; (b) TEM-DF micrograph taken using a [100] B2 superlattice reflection; (c) low-magnification, two-beam TEM-BF micrograph showcasing an overview of the deformed microstructure with long dislocation segments in A2 channels, many of them possessing cross slip like features (yellow arrows); (d,e) a representative dislocation imaged along the [001] and [113] ZA, with trace analysis shown in (d) confirming multiple cross-slip events and (f) its schematic representation showing respective slip planes and Burgers vector; (g) TEM-BF micrograph along a [113] ZA illustrating various dislocation-precipitate interactions, including climb (blue arrows).

3.4.4 | A2/B2 Interface Post Creep

The stability of the matrix-precipitate interface is a key factor influencing the creep behavior of precipitation-strengthened alloys. To examine the nature and coherency of the A2/B2 interface, high-resolution STEM-HAADF experiments were performed on a specimen crept at 1030°C and 125 MPa. Micrographs were acquired along a [001] ZA from different interface locations, as indicated in Figure 9a. Atomic resolution images of these regions are shown in Figure 9b_1–d_1, with the corresponding inverse FFT images in Figure 9b_2–d_2, obtained using masked $(110)_{A2,B2}$ spots, as shown in Figure 9b_3.

The continuity of the (110) planes across multiple interface regions demonstrates that the A2/B2 interfaces remain fully coherent, even after rafting under this creep condition. This observation is consistent with similar coherency observed in the specimen crept at 150 MPa (not shown), as well as with previous studies on undeformed specimens annealed for up to 1000 h [40], indicating that the inherent stability of the A2/B2 interface is maintained across diverse conditions.

The preservation of interfacial coherency implies that the changes in dislocation behavior observed across different stress levels (low to high) are not associated with a loss of interface coherency but rather arise from variations in dislocation activity within a structurally stable two-phase microstructure.

3.5 | Linking Microstructural Evolution to Creep Behavior

The creep tests were conducted at 1030°C under applied stresses of 100, 125, and 150 MPa, corresponding to the low-, intermediate-, and high-stress conditions, respectively.

At 100 MPa (low-stress), the creep test was interrupted before the onset of secondary creep. The resulting microstructure (Figure 6) exhibits a low dislocation density and well-developed ⟨100⟩-rafted B2 precipitates, with occasional climb events (Figure 6d) enabling dislocations to bypass the precipitates. No evidence of B2 precipitate cutting is observed at this stress level, indicating that dislocations likely bypass B2 precipitates via climb. This interpretation is consistent with the relatively low apparent stress exponent (approximately 3.5), although the underlying creep mechanism cannot be conclusively established from this value alone.

At 125 MPa (transition stress), the specimen exhibits a prolonged steady-state creep region accompanied by markedly increased dislocation activity. While dislocation climb is still observed, additional features suggest cutting of B2 precipitates by paired dislocations (Figure 7d,e). These paired segments correspond to strongly coupled superpartials cutting through the ordered B2 phase in a coordinated manner, consistent with behavior previously reported for room-temperature deformation [40].

It is well established that the elastic modulus is retained to approximately 75% of its room temperature value at a homologous temperature of $T_{hom} \sim 0.52$ at 1030°C [66], leading to a reduction in dislocation line tension. For an applied normal stress of 125 MPa (approximately 41 MPa in shear stress, using a Taylor factor of 3.06 [40]), the γ_{APB} at 1030°C must decrease to approximately 60% compared to room temperature to yield a comparable critical shear stress (see Figure S9 for an estimation of τ_{HR} using the Hüther and Reppich model) [67]. This level of reduction is reasonable, as previous work on B2 Fe_3Al reports a approximately 24% decrease in γ_{APB} at a lower homologous temperature ($T_{hom} \sim 0.38$) [68]. Under these conditions, the B2 precipitates are expected to be cut, consistent with the present TEM observations (Figure 7d,e).

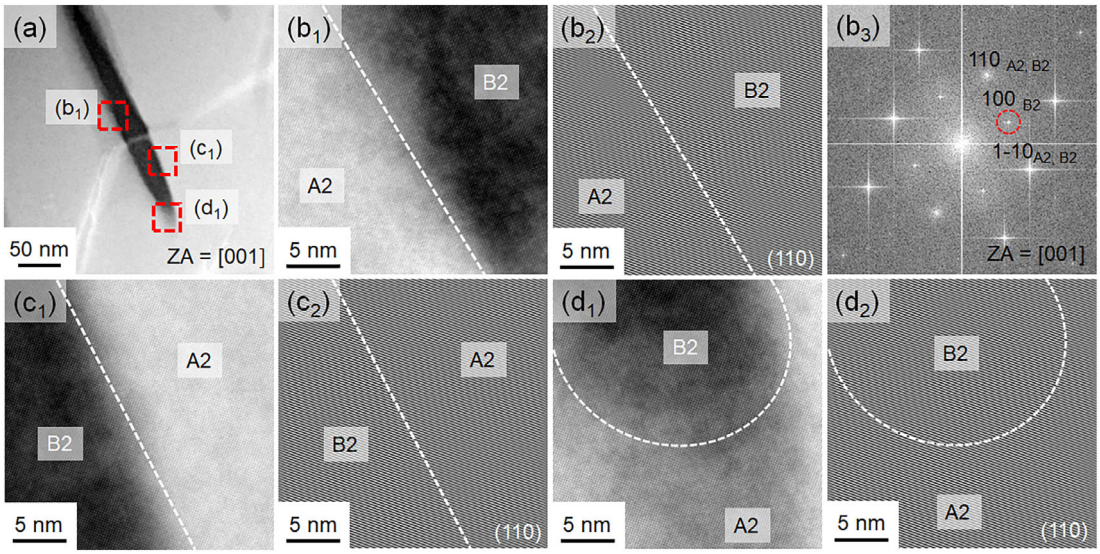

FIGURE 9 | Nature of the interface between the A2 matrix and B2 precipitates in the specimen that was crept at 1030°C under 125 MPa to a strain of 3.1%. (a) Low-magnification HAADF–STEM micrograph showing an elongated, rafted B2 precipitate within the A2 matrix; (b_1, c_1, and d_1) high-resolution HAADF–STEM micrographs of different sections of the precipitate-matrix interface, as indicated in (a); (b_2, c_2, and d_2) Corresponding inverse fast Fourier transform (IFFT) images obtained using the (110) spots from the FFT patterns. One representative FFT pattern corresponding to Figure (b_1) is shown in Figure (b_3).

The microstructure also contains several long dislocations on {110} or {112} within the A2 channels (Figure 7g), likely possessing a screw (or mixed) character, as commonly observed in BCC alloys [69–72]. In addition, the increased stress led to more intense dislocation–precipitate interaction. Several dislocation segments near the precipitate (Figure 7 and Figure S4), resembling the configuration shown in Figure 6d (low-stress conditions), are observed in the TEM micrographs, which indicates the frequent occurrence of dislocation climb in addition to the aforementioned cutting. Similarly, the jogged screw dislocations require thermally activated climb to move. However, the relative contributions of these mechanisms cannot be quantified due to practical limitations and the unavailability of crucial parameters at high temperatures.

At 150 MPa (high-stress), the creep response appears to be governed by extensive cross slip of screw dislocations between {110} and {112} (Figure 8c–d). Some climb events are still observed (Figure 8f), but they are comparatively rare. Notably, no evidence of B2 precipitate cutting is observed at this stress level, suggesting that repeated cross slip is the prominent feature of the dislocation activity.

Across all stress conditions, the B2 precipitates exhibit consistent rafting along the ⟨100⟩ direction. As rafting progresses, coalescence reduces the interparticle spacing (Figure 6b), thereby increasing the Orowan stress required for dislocation bypass [73] and making looping unlikely. To check this in the same manner, the Orowan stress (τ_{Orowan}) was estimated using ($\tau_{\mathrm{Orowan}} \approx 0.4Gb/\lambda$) [74, 75] for the channel widths (λ) measured in this study (in Section S10 in the Supplementary Materials). Applying a temperature-corrected shear modulus (approximately 60 GPa), the calculated Orowan shear stresses range from approximately 52 to 71 MPa. Converted to normal stresses using a Taylor factor of 3.06 [40], these values (approximately 159–217 MPa) exceed the applied creep stresses (100–150 MPa). Since the applied stresses (100–150 MPa) are below the estimated Orowan stress, the absence of Orowan loops in TEM observations is plausible.

At 150 MPa, the high Orowan stress may favor cross slip events, and TEM micrographs (Figure 8c–d) confirm multiple cross slip of screw dislocations between {110} and {112} planes, indicating that creep at 150 MPa is possibly dominated by cross-slip-mediated glide. This observation is consistent with the broader understanding that thermally activated glide governs creep in the power-law breakdown regime of polycrystalline materials [76, 77]. Nonetheless, due to the limited field of view in TEM, additional deformation pathways on larger scales cannot be entirely ruled out. For instance, the dynamic recovery processes associated with the formation of low-misorientation subgrain structures under all investigated conditions (as noted in Section 3.3).

All the creep deformation characteristics discussed above correspond to tests carried out at 1030°C, which is $\sim 0.52T_{\mathrm{solidus}}$ ($T_{\mathrm{solidus}} \sim 2250$°C) and $\sim 0.98T_{\mathrm{solvus}}$ of the precipitate solvus temperature [4, 21]. Therefore, the observations reported here are very close to the solvus temperature. At lower temperatures, slower diffusion would reduce climb bypass, and precipitate cutting might become the operating mechanism, as commonly observed in γ'-strengthened Ni-base alloys [16, 17, 78]. Meanwhile, cross slip would still be prevalent in the A2 channels; however, whether dislocations could escape to the adjacent A2 channel would depend on rafting kinetics, interparticle spacing along the rafting direction, and the applied stress. To fully map these mechanisms, transitions would require a systematic investigation over a wide temperature–stress range. The stress and temperature ranges selected in the present study are substantially restricted, not only by practical considerations of test duration but also by the brittleness of the alloy. Higher stresses (>175 MPa) are not possible due to brittle materials' response and premature failure by increased strain rates. Lower temperatures will further restrict the accessible parameter range.

As the creep properties are comparable to, or even superior to, those of some state-of-the-art Ni-based superalloys [21], it is essential to compare their dislocation activity as well. Unlike precipitation-strengthened Ni-based superalloys, which commonly develop extensive dislocation networks during creep [10, 16, 17, 79], the TMT-10Al-8Cr alloy shows no such network formation close to the precipitate–matrix interface. These observations may be rationalized by several factors. First, the misfit between B2 particles and A2 matrix is found here to be slightly positive or close to zero [4, 21], whereas it is commonly found to be negative in γ'-strengthened Ni-based superalloys (for example, (−0.1 to 0.3)% in CMSX-4 [80–82]). Second, creep deformation in TMT-8Cr-10Al has been rather small (less than 5% at 125 and 150 MPa); at 100 MPa, the material just entered steady state at a very small creep strain (0.6%). Additionally, the restricted motion of the jogged screw dislocations [60] prevents extensive dislocation–dislocation interaction in the A2 channels. To conclude, the dislocation activity in TMT-10Al-8Cr contrasts strongly with that in Ni-based superalloys.

4 | Conclusions

This study builds on our previous work, which established that the TMT-8Cr-10Al alloy exhibits two distinct creep regions at 1030°C, with a critical transition occurring near 125 MPa. However, the specific microstructural changes and dislocation-precipitate interactions across this stress range remained unresolved. Within this context, the main contributions of the present work are:

1. 3D morphology of rafted B2 precipitates: FIB-based quasi-3D representation reveals, for the first time, the true spatial morphology of the rafted B2 precipitates, which form laterally continuous but vertically separated as plate-like structures.
2. Subgrain structure formation: Under all investigated conditions, low-misorientation subgrain structures were observed via EBSD. This development, consistent with dynamic recovery processes, resulted from the rearrangement of dislocations into energetically favorable configurations.
3. Stress-dependent evolution of dislocation–precipitate interactions at 1030°C: TEM observations reveal a clear stress-dependent evolution of dislocation configurations

and dislocation–precipitate interactions. At low stress (100 MPa), the observed dislocation configurations are consistent with climb-assisted bypass of B2 precipitates. At 125 MPa, a transition from low to high stress region is identified, characterized by the coexistence of multiple interaction modes, including climb-assisted bypass, jogged-screw dislocations, and precipitate cutting by paired dislocations. At high stress (150 MPa), dislocation activity is dominated by long screw segments exhibiting frequent cross slip, while no evidence of precipitate cutting is observed.

4. Post-creep A2/B2 interface stability: High-resolution STEM-HAADF analysis confirms that the A2/B2 interfaces remain fully coherent across all creep conditions examined, indicating that the observed changes in dislocation behavior occur within a structurally stable two-phase microstructure.

Author Contributions

Liu Yang: writing – original draft, writing – review & editing, visualization, validation, methodology, investigation, formal analysis, data curation, conceptualization. **Aparajita Pramanik:** writing – original draft, writing – review & editing, visualization, validation, methodology, investigation, formal analysis, data curation, conceptualization. **Sandipan Sen:** writing – original draft, writing – review & editing, visualization, validation. methodology, investigation, formal analysis, conceptualization. **Shubhashis Dixit:** writing – original draft, writing – review & editing, visualization, investigation, validation, methodology, formal analysis, conceptualization. **Marcel Münch:** writing – review & editing, data curation, visualization, investigation, conceptualization. **R. J. Vikram:** writing – original draft, writing – review & editing, visualization, investigation, validation, methodology, formal analysis, conceptualization. **Daniel Schliephake:** writing – review & editing, visualization, resources, investigation. **Yolita M. Eggeler:** writing – review & editing, visualization, investigation. **Ankur Chauhan:** writing – original draft, writing – review & editing, methodology, alidation, supervision, project administration, funding acquisition, formal analysis, resources. **Martin Heilmaier:** supervision, resources, writing – review & editing, funding acquisition, methodology, formal analysis, visualization, validation, conceptualization. **Alexander Kauffmann:** writing – original draft, writing – review & editing, investigation, methodology, formal analysis, project administration, funding acquisition, data curation, visualization, validation, supervision, conceptualization.

Acknowledgments

We gratefully acknowledge financial support from the Deutsche Forschungsgemeinschaft (DFG), grant no. HE 1872/34–2. This work was partly carried out with the support of the Karlsruhe Nano Micro Facility (KNMFi, grant no. 2025–034 032388), a Helmholtz Research Infrastructure at Karlsruhe Institute of Technology (KIT, grant no. 2025–034 032388). LY acknowledges financial support from the China Scholarship Council (CSC), grant no. 202207000023. RJV acknowledges the support of the Alexander von Humboldt Foundation. MM acknowledges financial support from the Landesgraduiertenförderung (LGF) of the state of Baden-Württemberg (Germany). AP and AC acknowledge the Advanced Facility for Microscopy and Microanalysis (AFMM) and its staff at the IISc, Bengaluru, for providing access to the characterization facilities. AC gratefully acknowledges financial support from the Infosys Foundation, Bangalore.

Open Access funding enabled and organized by Projekt DEAL.

Funding

This study was supported by the Deutsche Forschungsgemeinschaft (HE 1872/34-2), Ministerium für Wissenschaft, Forschung und Kunst Baden-Württemberg, Chinese Government Scholarship (202207000023), Karlsruhe Nano Micro Facility for Information-driven Material Structuring and Characterization (KNMFi) (2025-034 032388), and Infosys Foundation.

Conflict of Interest

The authors declare no conflicts of interest.

Data Availability Statement

The data presented in this study are available at https://doi.org/10.5281/zenodo.20021746 under CC BY-SA 4.0 license. Further information is available upon request with sandipan.sen@kit.edu, and alexander.kauffmann@rub.de.

References

1. O. N. Senkov, G. B. Wilks, D. B. Miracle, C. P. Chuang, and P. K. Liaw, "Refractory High-Entropy Alloys," *Intermetallics* 18 (2010): 1758–1765, https://doi.org/10.1016/j.intermet.2010.05.014.

2. H. W. Yao, J. W. Qiao, J. A. Hawk, H. F. Zhou, M. W. Chen, and M. C. Gao, "Mechanical Properties of Refractory High-Entropy Alloys: Experiments and Modeling," *Journal of Alloys and Compounds* 696 (2017): 1139–1150, https://doi.org/10.1016/j.jallcom.2016.11.188.

3. O. N. Senkov and C. F. Woodward, "Microstructure and Properties of a Refractory $NbCrMo_{0.5}Ta_{0.5}TiZr$ Alloy," *Materials Science and Engineering: A* 529 (2011): 311–320, https://doi.org/10.1016/j.msea.2011.09.033.

4. R. J. Vikram, S. Sen, L. Yang, et al., "Ultra-Slow Coarsening in Precipitation-Strengthened Refractory High-Entropy Alloys," *Scripta Materialia* 271 (2026): 117026, https://doi.org/10.1016/j.scriptamat.2025.117026.

5. O. N. Senkov, G. B. Wilks, J. M. Scott, and D. B. Miracle, "Mechanical Properties of $Nb_{25}Mo_{25}Ta_{25}W_{25}$ and $V_{20}Nb_{20}Mo_{20}Ta_{20}W_{20}$ Refractory High Entropy Alloys," *Intermetallics* 19 (2011): 698–706, https://doi.org/10.1016/j.intermet.2011.01.004.

6. M. Wang, Z. Ma, Z. Xu, and X. Cheng, "Microstructures and Mechanical Properties of HfNbTaTiZrW and HfNbTaTiZrMoW Refractory High-Entropy Alloys," *Journal of Alloys and Compounds* 803 (2019): 778–785, https://doi.org/10.1016/j.jallcom.2019.06.138.

7. C. Panwisawas, H. Mathur, J.-C. Gebelin, D. Putman, C. M. F. Rae, and R. C. Reed, "Prediction of Recrystallization in Investment Cast Single-Crystal Superalloys," *Acta Materialia* 61 (2013): 51–66, https://doi.org/10.1016/j.actamat.2012.09.013.

8. D. Bürger, A. B. Parsa, M. Ramsperger, C. Körner, and G. Eggeler, "Creep Properties of Single Crystal Ni-Base Superalloys (SX): A Comparison between Conventionally Cast and Additive Manufactured CMSX-4 Materials," *Materials Science and Engineering A* 762 (2019), https://doi.org/10.1016/j.msea.2019.138098.

9. R. C. Reed, *The Superalloys: Fundamentals and Applications* (Cambridge University Press, 2008).

10. P. Wollgramm, H. Buck, K. Neuking, et al., "On the Role of Re in the Stress and Temperature Dependence of Creep of Ni-Base Single Crystal Superalloys," *Materials Science and Engineering: A* 628 (2015): 382–395, https://doi.org/10.1016/j.msea.2015.01.010.

11. A. Epishin, B. Fedelich, G. Nolze, et al., "Creep of Single Crystals of Nickel-Based Superalloys at Ultra-High Homologous Temperature," *Metallurgical and Materials Transactions A* 49 (2018): 3973–3987, https://doi.org/10.1007/s11661-018-4729-6.

12. C.-J. Liu, C. Gadelmeier, S.-L. Lu, et al., "Tensile Creep Behavior of HfNbTaTiZr Refractory High Entropy Alloy at Elevated Temperatures," *Acta Materialia* 237 (2022): 118188, https://doi.org/10.1016/j.actamat.2022.118188.

13. C. Gadelmeier, Y. Yang, U. Glatzel, and E. P. George, "Creep Strength of Refractory High-Entropy Alloy TiZrHfNbTa and Comparison with Ni-Base Superalloy CMSX-4," *Cell Reports Physical Science* 3 (2022): 100991, https://doi.org/10.1016/j.xcrp.2022.100991.

14. M. Vaidya, S. Trubel, B. S. Murty, G. Wilde, and S. V. Divinski, "Ni Tracer Diffusion in CoCrFeNi and CoCrFeMnNi High Entropy Alloys," *Journal of Alloys and Compounds* 688 (2016): 994–1001, https://doi.org/10.1016/j.jallcom.2016.07.239.

15. J. Zhang, C. Gadelmeier, S. Sen, et al., "Zr Diffusion in BCC Refractory High Entropy Alloys: A Case of Non-Sluggish Diffusion Behavior," *Acta Materialia* 233 (2022): 117970, https://doi.org/10.1016/j.actamat.2022.117970.

16. L. A. Jácome, P. Nörtershäuser, C. Somsen, A. Dlouhý, and G. Eggeler, "On the Nature of γ' Phase Cutting and Its Effect on High Temperature and Low Stress Creep Anisotropy of Ni-Base Single Crystal Superalloys," *Acta Materialia* 69 (2014): 246–264, https://doi.org/10.1016/j.actamat.2014.01.021.

17. S. M. H. Haghighat, G. Eggeler, and D. Raabe, "Effect of Climb on Dislocation Mechanisms and Creep Rates in γ'-Strengthened Ni Base Superalloy Single Crystals: A Discrete Dislocation Dynamics Study," *Acta Materialia* 61 (2013): 3709–3723, https://doi.org/10.1016/j.actamat.2013.03.003.

18. S. Laube, A. Kauffmann, S. Schellert, et al., "Formation and Thermal Stability of Two-Phase Microstructures in Al-Containing Refractory Compositionally Complex Alloys," *Science and Technology of Advanced Materials* 23 (2022): 692–706, https://doi.org/10.1080/14686996.2022.2132118.

19. S. Laube, S. Schellert, A. S. Tirunilai, et al., "Microstructure Tailoring of Al-Containing Compositionally Complex Alloys by Controlling the Sequence of Precipitation and Ordering," *Acta Materialia* 218 (2021): 117217, https://doi.org/10.1016/j.actamat.2021.117217.

20. O. N. Senkov, B. Crossman, S. I. Rao, et al., "Mechanical Properties of an $Al_{10}Nb_{20}Ta_{15}Ti_{30}V_5Zr_{20}$ A2/B2 Refractory Superalloy and its Constituent Phases," *Acta Materialia* 254 (2023): 119017, https://doi.org/10.1016/j.actamat.2023.119017.

21. L. Yang, S. Sen, D. Schliephake, et al., "Creep Behavior of a Precipitation-Strengthened A2-B2 Refractory High Entropy Alloy," *Acta Materialia* 288 (2025): 120827, https://doi.org/10.1016/j.actamat.2025.120827.

22. D. K. Matlock and W. D. Nix, "The Effect of Sample Size on the Steady State Creep Characteristics of Ni-6 pct W," *Metallurgical Transactions* 5 (1974): 1401–1412, https://doi.org/10.1007/BF02646626.

23. M. Heilmaier, M. Krüger, H. Saage, et al., "Metallic Materials for Structural Applications Beyond Nickel-Based Superalloys," *JOM* 61 (2009): 61–67, https://doi.org/10.1007/s11837-009-0106-7.

24. A. Bauer, S. Neumeier, F. Pyczak, R. F. Singer, and M. Göken, "Creep Properties of Different γ'-Strengthened Co-Base Superalloys," *Materials Science and Engineering: A* 550 (2012): 333–341, https://doi.org/10.1016/j.msea.2012.04.083.

25. A. Bauer, S. Neumeier, F. Pyczak, and M. Göken, "Creep Strength and Microstructure of Polycrystalline γ'-Strengthened Cobalt-Base Superalloys," *Superalloys* 12 (2012): 695–703, https://doi.org/10.7449/2012/Superalloys_2012_695_703.

26. T. Tsuru, S. Han, S. Matsuura, et al., "Intrinsic Factors Responsible for Brittle Versus Ductile Nature of Refractory High-Entropy Alloys," *Nature Communications* 15 (2024): 1706, https://doi.org/10.1038/s41467-024-45639-8.

27. J.-P. Couzinié, L. Lilensten, Y. Champion, G. Dirras, L. Perrière, and I. Guillot, "On the Room Temperature Deformation Mechanisms of a TiZrHfNbTa Refractory High-Entropy Alloy," *Materials Science and Engineering: A* 645 (2015): 255–263, https://doi.org/10.1016/j.msea.2015.08.024.

28. O. N. Senkov, J. M. Scott, S. V. Senkova, D. B. Miracle, and C. F. Woodward, "Microstructure and Room Temperature Properties of a High-Entropy TaNbHfZrTi Alloy," *Journal of Alloys and Compounds* 509 (2011): 6043–6048, https://doi.org/10.1016/j.jallcom.2011.02.171.

29. K.-K. Tseng, H.-H. Huang, W.-R. Wang, J.-W. Yeh, and C.-W. Tsai, "Edge-Dislocation-Induced Ultrahigh Elevated-Temperature Strength of HfMoNbTaW Refractory High-Entropy Alloys," *Science and Technology of Advanced Materials* 23 (2022): 642–654, https://doi.org/10.1080/14686996.2022.2129444.

30. Z. Li, B. Su, C. Liu, R. Chen, L. Wang, and Y. Su, "Tuning Deformation Mechanisms in Refractory High-Entropy Alloys: Slip Plane Preference and Dislocation Behavior," *International Journal of Plasticity* 192 (2025): 104424, https://doi.org/10.1016/j.ijplas.2025.104424.

31. G. Sahragard-Monfared, C. H. Belcher, S. Bajpai, et al., "Tensile Creep Behavior of the $Nb_{45}Ta_{25}Ti_{15}Hf_{15}$ Refractory High Entropy Alloy," *Acta Materialia* 272 (2024): 119940, https://doi.org/10.1016/j.actamat.2024.119940.

32. K. Ma, T. Blackburn, J. P. Magnussen, et al., "Chromium-Based bcc-Superalloys Strengthened by Iron Supplements," *Acta Materialia* 257 (2023): 119183, https://doi.org/10.1016/j.actamat.2023.119183.

33. A. J. Knowles, T.-S. Jun, A. Bhowmik, et al., "A New Beta Titanium Alloy System Reinforced With Superlattice Intermetallic Precipitates," *Scripta Materialia* 140 (2017): 71–75, https://doi.org/10.1016/j.scriptamat.2017.06.038.

34. R. D. Noebe, R. R. Bowman, and M. V. Nathal, "Physical and Mechanical Properties of the B2 Compound NiAl," *International Materials Reviews* 38 (2013): 193–232, https://doi.org/10.1179/imr.1993.38.4.193.

35. M. Yamaguchi and Y. Umakoshi, "The Deformation Behaviour of Intermetallic Superlattice Compounds, Progress in Materials Science 34 (1990): 1–148, https://doi.org/10.1016/0079-6425(90)90002-Q.

36. H. L. Fraser, M. H. Loretto, and R. E. Smallman, "The Plastic Deformation of NiAl Single Crystals Between 300°K and 1050°K: II. The Mechanism of Kinking and Uniform Deformation," *Philosophical Magazine A* 28 (2006): 667–677, https://doi.org/10.1080/14786437308221010.

37. M. Yoshida and T. Takasugi, "Transmission Electron Microscopy Study of the Activated Slip Systems and the Dislocation Structures in B2-Type CoZr and CoHf Polycrystals," *Philosophical Magazine A* 68 (1993): 401–417, https://doi.org/10.1080/01418619308221212.

38. J. Wang, A. Barooni, and M. Ghazisaeidi, "Stability of the B2 Phase Among Refractory Metals," *Acta Materialia* 279 (2024): 120323, https://doi.org/10.1016/j.actamat.2024.120323.

39. J.-P. Couzinié, G. Viswanathan, V. Soni, R. Banerjee, H. L. Fraser, and M. J. Mills, "Unveiling the Deformation Mechanisms of BCC-Superalloys," *Scripta Materialia* 267 (2025): 116801, https://doi.org/10.1016/j.scriptamat.2025.116801.

40. A. Pramanik, C. Konkati, S. Laube, et al., "Exploring Room-Temperature Deformation Mechanisms of a B2-Strengthened Refractory Compositionally Complex Alloy," *Materials Science and Engineering: A* 931 (2025): 148180, https://doi.org/10.1016/j.msea.2025.148180.

41. A. K. Mukherjee, J. E. Bird, and J. E. Dorn, "Experimental Correlations for High-Temperature Creep," *Transactions of the Metallurgical Society of AIME* 242 (1969): 1559–1566.

42. N. Yurchenko, E. Panina, Ł. Rogal, L. Shekhawat, S. Zherebtsov, and N. Stepanov, "Unique Precipitations in a Novel Refractory Nb-Mo-Ti-Co High-Entropy Superalloy," *Materials Research Letters* 10 (2022): 78–87, https://doi.org/10.1080/21663831.2021.2022033.

43. C. H. Belcher, D. Kamp, S. To, et al., "The Origin and Control of Interstitial Impurities in Refractory Complex Concentrated Alloys," *Journal of Alloys and Compounds* 1010 (2025): 177520, https://doi.org/10.1016/j.jallcom.2024.177520.

44. F. R. M. Nabarro, "Grain Size, Stress, and Creep in Polycrystalline Solids," *Physics of the Solid State* 42 (2000): 1456–1459, https://doi.org/10.1134/1.1307052.

45. R. Lagneborg and B. Bergman, "The Stress/Creep Rate Behaviour of Precipitation-Hardened Alloys," *Metal Science* 10 (2013): 20–28, https://doi.org/10.1179/030634576790431462.

46. A. J. Ardell, "Precipitation Hardening," *Metallurgical Transactions A* 16 (1985): 2131–2165, https://doi.org/10.1007/BF02670416.

47. M. Kamaraj, C. Mayr, M. Kolbe, and G. Eggeler, "On the Influence of Stress State on Rafting in the Single Crystal Superalloy CMSX-6 Under Conditions of High Temperature and Low Stress Creep," *Scripta Materialia* 38 (1998): 589–594, https://doi.org/10.1016/S1359-6462(97)00520-4.

48. A. Argon, *Strengthening Mechanisms in Crystal Plasticity* (Oxford University Press, 2007).

49. E. Arzt and D. S. Wilkinson, "Threshold Stresses for Dislocation Climb Over Hard Particles: The Effect of an Attractive Interaction," *Acta Metallurgica* 34 (1986): 1893–1898, https://doi.org/10.1016/0001-6160(86)90247-6.

50. J. Rösler and E. Arzt, "The Kinetics of Dislocation Climb Over Hard Particles—I. Climb Without Attractive Particle-Dislocation Interaction," *Acta Metallurgica* 36 (1988): 1043–1051, https://doi.org/10.1016/0001-6160(88)90158-7.

51. E. A. Marquis and D. C. Dunand, "Model for Creep Threshold Stress in Precipitation-Strengthened Alloys With Coherent Particles," *Scripta Materialia* 47 (2002): 503–508, https://doi.org/10.1016/S1359-6462(02)00165-3.

52. S. M. Zhu, S. C. Tjong, and J. K. L. Lai, "Creep Behavior of a β′(NiAl) Precipitation Strengthened Ferritic Fe–Cr–Ni–Al Alloy," *Acta Materialia* 46 (1998): 2969–2976, https://doi.org/10.1016/S1359-6454(98)00022-6.

53. N. Q. Vo, C. H. Liebscher, M. J. S. Rawlings, M. Asta, and D. C. Dunand, "Creep Properties and Microstructure of a Precipitation-Strengthened Ferritic Fe–Al–Ni–Cr Alloy," *Acta Materialia* 71 (2014): 89–99, https://doi.org/10.1016/j.actamat.2014.02.020.

54. Y. Zhao, Q. Fang, Y. Liu, P. Wen, and Y. Liu, "Creep Behavior as Dislocation Climb Over NiAl Nanoprecipitates in Ferritic Alloy: The Effects of Interface Stresses and Temperature," *International Journal of Plasticity* 69 (2015): 89–101, https://doi.org/10.1016/j.ijplas.2015.02.006.

55. M. J. S. Rawlings, C. H. Liebscher, M. Asta, and D. C. Dunand, "Effect of Titanium Additions Upon Microstructure and Properties of Precipitation-Strengthened Fe-Ni-Al-Cr Ferritic Alloys," *Acta Materialia* 128 (2017): 103–112, https://doi.org/10.1016/j.actamat.2017.02.028.

56. S.-I. Baik, S.-Y. Wang, P. K. Liaw, and D. C. Dunand, "Increasing the Creep Resistance of Fe-Ni-Al-Cr Superalloys via Ti Additions by Optimizing the B2/L21 Ratio in Composite Nano-Precipitates," *Acta Materialia* 157 (2018): 142–154, https://doi.org/10.1016/j.actamat.2018.07.025.

57. E. Arzt and M. F. Ashby, "Threshold Stresses in Materials Containing Dispersed Particles," *Scripta Metallurgica* 16 (1982): 1285–1290.

58. W. Blum and B. Reppich, *Creep of Particle-Strengthened Alloys, in: Creep Behaviour of Crystalline Solids* (Pineridge Press, 1985). 83–135.

59. S. Karthikeyan, G. B. Viswanathan, and M. J. Mills, "Evaluation of the Jogged-Screw Model of Creep in Equiaxed γ-TiAl: Identification of the Key Substructural Parameters," *Acta Materialia* 52 (2004): 2577–2589, https://doi.org/10.1016/j.actamat.2004.02.006.

60. G. B. Viswanathan, R. W. Hayes, and M. J. Mills, "A Study Based on Jogged-Screw Dislocations for High Temperature Creep in Ti Alloys," *Materials Science and Engineering: A* 319 (2001): 706–710, https://doi.org/10.1016/S0921-5093(01)01048-6.

61. M. Wilkens and E. Hornbogen, "Kontrasterscheinungen an Versetzungspaaren in Nickel–Aluminium-Legierungen Mit Kohärenter Ausscheidung Von Geordneten Bereichen," *physica status solidi (b)* 4 (1964): 557–568, https://doi.org/10.1002/pssb.19640040309.

62. S. Zhang, D. E. Mikkola, and W. W. Milligan, "APB vs. SISF Dissociation of Superdislocations in Cubic $L1_2$ Al_3Ti Alloys," *Scripta Metallurgica et Materialia* 27 (1992): 1073–1077, https://doi.org/10.1016/0956-716X(92)90476-U.

63. T. M. Pollock and R. D. Field, *Chapter 63 Dislocations and High-Temperature Plastic Deformation of Superalloy Single Crystals, in: Dislocations in Solids* (Elsevier, 2002), 547–618, https://doi.org/10.1016/S1572-4859(02)80014-6.

64. M. F. Ashby, "A First Report on Deformation-Mechanism Maps," *Acta Metallurgica* 20 (1972): 887–897, https://doi.org/10.1016/0001-6160(72)90082-X.

65. F. Sun, Y. F. Gu, J. B. Yan, Z. H. Zhong, and M. Yuyama, "Phenomenological and Microstructural Analysis of Intermediate Temperatures Creep in a Ni–Fe-Based Alloy for Advanced Ultra-Supercritical Fossil Power Plants," *Acta Materialia* 102 (2016): 70–78, https://doi.org/10.1016/j.actamat.2015.09.006.

66. W. Köster, "Die Temperaturabhängigkeit Des Elastizitätsmoduls Reiner Metalle," *International Journal of Materials Research* 39 (1948): 1–9, https://doi.org/10.1515/ijmr-1948-390101.

67. B. Reppich, "Particle Strengthening," *Materials Science and Technology* 6 (1993): 311–357.

68. M. Friák, M. Černý, and M. Šob, "Temperature-Dependent Impact of Antiphase Boundaries on Properties of Fe_3Al," *Intermetallics* 151 (2022): 107746, https://doi.org/10.1016/j.intermet.2022.107746.

69. S. Takeuchi, E. Furubayashi, and T. Taoka, "Orientation Dependence of Yield Stress in 4.4% Silicon Iron Single Crystals," *Acta Metallurgica* 15 (1967): 1179–1191, https://doi.org/10.1016/0001-6160(67)90392-6.

70. J. W. Christian, "Some Surprising Features of the Plastic Deformation of Body-Centered Cubic Metals and Alloys," *Metallurgical Transactions A* 14 (1983): 1237–1256, https://doi.org/10.1007/BF02664806.

71. R. J. Arsenault and A. Lawley, "Work Hardening and Dislocation Structure in Ta and Ta-Base Alloys," *Philosophical Magazine A* 15 (2006): 549–565, https://doi.org/10.1080/14786436708220902.

72. F. Maresca and W. A. Curtin, "Theory of Screw Dislocation Strengthening in Random BCC Alloys From Dilute to "High-Entropy" Alloys," *Acta Materialia* 182 (2020): 144–162, https://doi.org/10.1016/j.actamat.2019.10.007.

73. Y. Li, Z. Tan, X. Wang, et al., "Identification of Intrinsic Mechanisms and Controlling Factors for γ′ Rafting of Ni-Based Single Crystal Superalloys," *Materials Research Letters* 13 (2025): 292–299, https://doi.org/10.1080/21663831.2024.2447291.

74. E. Orowan, *Internal Stresses in Metals and Alloys, in: Symposium on Internal Stresses in Metals and Alloys* (Institute of Metals, 1948), 451–453.

75. D. J. Bacon, U. F. Kocks, and R. O. Scattergood, "The Effect of Dislocation Self-Interaction on the Orowan Stress," *Philosophical Magazine* 28 (1973): 1241–1263, https://doi.org/10.1080/14786437308227997.

76. M. E. Kassner, *Fundamentals of Creep in Metals and Alloys* (Butterworth-Heinemann, 2015).

77. S. V. Raj, I. Seideniskovitz, and A. D. Freed, "Modeling the Role of Dislocation Substructure During Class M and Exponential Creep," in*Unified Constitutive Laws of Plastic Deformation*, ed. A. S. Krausz and K. Krausz (Academic Press, 1995), 343–439.

78. Q. Yue, L. Liu, W. Yang, et al., "Stress Dependence of the Creep Behaviors and Mechanisms of a Third-Generation Ni-Based Single Crystal Superalloy," *Journal of Materials Science & Technology* 35 (2019): 752–763, https://doi.org/10.1016/j.jmst.2018.11.015.

79. X. Wu, P. Wollgramm, C. Somsen, A. Dlouhy, A. Kostka, and G. Eggeler, "Double Minimum Creep of Single Crystal Ni-Base Superalloys," *Acta Materialia* 112 (2016): 242–260, https://doi.org/10.1016/j.actamat.2016.04.012.

80. R. Völkl, U. Glatzel, and M. Feller-Kniepmeier, "Measurement of the Lattice Misfit in the Single Crystal Nickel Based Superalloys CMSX-4, SRR99 and SC16 by Convergent Beam Electron Diffraction," *Acta Materialia* 46 (1998): 4395–4404, https://doi.org/10.1016/S1359-6454(98)00085-8.

81. U. Brückner, A. Epishin, T. Link, and K. Dressel, "The Influence of the Dendritic Structure on the $\frac{\gamma}{\gamma'}$-Lattice Misfit in the Single-Crystal Nickel-Base Superalloy CMSX-4," *Materials Science and Engineering: A* 247 (1998): 23–31, https://doi.org/10.1016/S0921-5093(97)00856-3.

82. J. Coakley, D. Ma, M. Frost, et al., "Lattice Strain Evolution and Load Partitioning During Creep of a Ni-Based Superalloy Single Crystal With Rafted γ' Microstructure," *Acta Materialia* 135 (2017): 77–87, https://doi.org/10.1016/j.actamat.2017.06.021.

Supporting Information

Additional supporting information can be found online in the Supporting Information section.